Atmospheric and Environmental Research, Inc.

840 Memorial Drive
Cambridge, Massachusetts
02139-3771

Telephone
617 547-6207

Facsimile
617 661-6479

www.aer.com

AER P599

Distortion Representation of Forecast Errors for Model Skill Assessment and Objective Analysis

A final report for NAS5-32953 submitted to:
National Aeronautics and Space Administration
Goddard Space Flight Center
Greenbelt MD 20771
For the period:
18 August 1995 - 17 August 1998

Submitted by
Atmospheric and Environmental Research, Inc.
Cambridge, MA 02139
15 September 1998

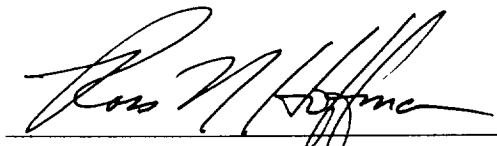

Dr. Ross N. Hoffman
Principal Investigator

The research described herein was supported by NASA contract NAS5-32953.

Atmospheric and Environmental Research (AER), Inc.,
840 Memorial Drive, Cambridge, MA 02139–3794.
Phone: +1 617 547 6207. Fax: +1 617 661 6479.
Net: `http://www.aer.com/`.

Contents

Summary

We proposed a novel characterization of errors for numerical weather predictions. A general distortion representation allows for the displacement and amplification or bias correction of forecast anomalies.

Characterizing and decomposing forecast error in this way has several important applications, including the model assessment application, and the objective analysis application. In this project we have focused on the assessment application, restricted to a realistic but univariate 2–dimensional situation. Specifically we study the forecast errors of the sea level pressure (SLP), the 500 hPa geopotential height, and the 315 K potential vorticity fields for forecasts of the short and medium range. The forecasts are generated by the GEOS (Goddard Earth Observing System) data assimilation system with and without ERS–1 scatterometer data.

A great deal of novel work has been accomplished under the current contract. In broad terms we have developed and tested an efficient algorithm for determining distortions. The algorithm and constraints are now ready for application to larger data sets, to be used to determine the statistics of the distortion as outlined above, and to be applied in data analysis by using GOES water vapor imagery to correct short term forecast errors.

1 Introduction

We proposed a novel characterization of errors for numerical weather predictions (Hoffman *et al.* 1995 [7]). In its simplest form we decompose the error into a part attributable to phase errors and a remainder. The phase error is represented in the same fashion as a velocity field and is required to vary slowly and smoothly with position. A general distortion representation allows for the displacement and amplification or bias correction of forecast anomalies (Hoffman and Grassotti 1996 [6]).

Characterizing and decomposing forecast error in this way has several important applications. For the model assessment application, our approach results in new objective measures of forecast skill which are more in line with subjective measures of forecast skill and which are useful in validating models and diagnosing their shortcomings. With regard to the objective analysis application, meteorological analysis schemes balance forecast error and observational error to obtain an optimal analysis. Presently, representations of the error covariance matrix used to measure the forecast error are severely limited. For the objective analysis application our approach will improve analyses by providing a more realistic measure of the forecast error. We expect, *a priori*, that our approach should greatly improve the utility of remotely sensed data which have relatively high horizontal resolution, but which are indirectly related to the conventional atmospheric variables (Hoffman and Grassotti 1996 [6]). A related application is to combine two sources of data, e.g. SSM/I and ground-based radar rain rates (Grassotti *et al.* 1998 [4]).

In this project we have focused on the assessment application, restricted to a realistic but univariate 2–dimensional situation. Specifically we study the forecast errors of the sea level pressure (SLP), the 500 hPa geopotential height, and the 315 K potential vorticity fields for forecasts of the short and medium range. The forecasts are generated by the GEOS (Goddard Earth Observing System) data assimilation system with and without ERS–1 scatterometer data. Our studies are a first step towards (1) a testbed for the use of the distortion representation of forecast errors, (2) a means of validating the GEOS data assimilation system and (3) a description of the impact of the ERS–1 scatterometer data.

This final report for NAS5-32953 is also offered in lieu of the annual report for the third and final year of the project. We report on the entire research project in this report. The particular areas of research studied during this past year are:

1. Extending the analysis to potential vorticity at 315 K. Examples are given of the March 1993 super storm.

2. Allowing for time continuity by treating the increment in C as the control variable to be constrained. (The C are the spectral representation of the distortion.)

3. Developing an approach to determine the statistics of the C.

4. Experimenting with different stopping criterion for the stepwise truncation part of our approach to determine the statistics of the C, in terms of isostropy and homogeniety.

5. Aquiring ECMWF Lorenz data sets of 500 hPa height. These data sets conviently provide large samples for determining the statistics of the C.

6. Developing an approach to use 6.7 μm water vapor imagery. To quality control cloud contamination we will use a window channel.

7. Aquiring OPTRAN and coefficients for GOES. GOES data are acquired routinely by AER for the northern hemisphere.

2 Data

Forecasts and verifying analyses made with the GEOS data assimilation and forecast system (Schubert *et al.* 1993 [20]) are used here. The particular experiments studied are described by Atlas *et al.* (1995 [1]) in a study of the impact of ERS–1 scatterometer data on numerical weather prediction. The period of study is March, 1993. The forecast model and data assimilation system used in these experiments are identical to the GEOS-1 system described by Schubert *et al.*, except for some minor bug fixes and the modifications necessary to utilize surface wind vectors. Thus the control forecasts in the impact study are standard GEOS forecasts. In addition to the CONTROL experiment, several using different types of scatterometer wind information are available. Our initial prototyping and sensitivity studies use only the $2 \times 2.5°$ CONTROL forecast for the period 6–11 March 1993. In addition we have made some comparisons to the corresponding PGLA and VARGLA forecasts. In all cases the CONTROL GEOS data assimilation is used as verification. The PGLA and VARGLA forecasts use the same setup as the CONTROL forecast, but both add ERS–1 scatterometer data to the CONTROL data sets in determining the initial conditions for the forecast. In PGLA the scatterometer data is processed using the directional filtering method of Offiler (1994 [12]), while in VARGLA, the variational analysis method of Hoffman (1984 [5]) is applied to the ERS–1 σ^0 measurements.

3 Methodology

Since we require that these distortion fields vary smoothly, a spectral representation is appropriate. Determining the distortion which provides the best match is then equivalent to minimizing the misfit between the first field and a distortion of the second, with respect to the spectral coefficients of the distortion. In the present project we use a global or hemispheric domain, and spherical harmonics as basis functions.

In brief, the distortion is determined by minimizing the objective function J, by varying the displacement and bias correction fields, where

$$J = J_r + J_d + J_a.$$

The residual cost function, J_r, measures the misfit of the distorted forecast to the verifying analysis. Minimizing J_r improves the agreement between the (distorted) forecast and the

analysis. The two additional penalty terms in the objective function, J_d and J_a, ensure that the final distortion produced by the minimization is relatively smooth and not too large. (The terms cost function, objective function and penalty function are used more or less interchangeably in the literature. Here, the objective function is the quantity to be minimized, a cost function measures lack of fit to data and a penalty function measures lack of fit to a constraint.) The smoothness penalty function, J_d measures the roughness of the x- and y-displacements and of the bias correction, ensuring that the distortion is large scale. The barrier penalty function, J_a, measures the magnitude of the distortion components in a way so that small distortions are not penalized, but large distortions are penalized heavily. This has the effect of setting up a barrier to the size of the distortions which are determined. These last two terms are evaluated using the spectral coefficients of the distortion.

The three terms making up J are described in the following sections. However, in our work so far, the spectral truncations used are so severe that J_d and J_a are not used in obtaining the results presented here. In our studies at the beginning of the project we found that using the barrier and smoothness penalty functions results in distortions which are smaller in magnitude, but larger in scale, and residual errors which are larger in scale and magnitude. The spectra of the original and residual forecast error, both with and without the penalty functions show that a great deal of the forecast error on the scales of the distortion is explained by the distortion and that the penalty constraints have a strong effect limiting the smallest scales in the distortion.

Note that the limits used to define J_a are found to be very useful to precondition the minimization, even in cases where J_a is not used in the functional. Simulation experiments demonstrated that if the control vector is scaled by its limiting values estimate, the true solution is quickly recovered. If the scaling is derived from the smoothing function instead, the minimization quickly fails with false convergence. For the case of uniform scaling of the control vector, the minimization is only partially successful: the objective function is reduced only slowly, and after 100 iterations, only half of the original forecast error is explained.

3.1 Residual cost function, J_r

The residual cost function J_r measures the misfit between the distorted forecast and the verifying analysis. We denote the forecast by F, the distorted forecast by P, and the verifying analysis, or what is considered truth, by T. The cost function is

$$J_r = \frac{\int_\sigma (P-T)^2 d\sigma}{\int_\sigma d\sigma},$$

where the integral is the surface integral over the global domain. The distorted forecast P is obtained from the unmodified forecast F by adding a location-dependent bias correction $B(\lambda,\theta)$ to the values displaced by the displacement vector field $\boldsymbol{D}(\lambda,\theta) = (D_u, D_v)$, where $\boldsymbol{D}$ is expressed here in terms of its zonal and meridional components, in analogy to a wind field. Thus, we may write

$$P(\lambda,\theta) = F(\lambda',\theta') + B(\lambda,\theta),$$

where the location (λ', θ') is found by following the displacement vector $\boldsymbol{D}(\lambda, \theta)$ back from its endpoint (λ, θ).

We represent the scalar field B by a truncated series of spherical harmonics, and the vector field $\boldsymbol{D}$ in terms of the spectral coefficients of the corresponding vorticity (ζ) and divergence (δ) fields. A degree of smoothness can thus easily be imposed by the truncation of the series, and further constraints can separately be imposed on the divergent and rotational parts of the displacement field. The control vector C for the optimization problem is thus composed of the spectral coefficients for B, ζ and δ:

$$C = (B, \zeta, \delta)^T.$$

Both the forecast F and the verifying analysis T are available on regular latitude-longitude grids. For evaluation of the integral, it is convenient to first interpolate T to a Gaussian latitude-longitude grid, in which case the formula for J_r takes the form

$$J_r = \sum_j \frac{w_j}{N_j} \sum_i (P_{ij} - T_{ij})^2,$$

where indices i, j denote the grid point location in longitude and latitude, N_j is the number of longitude points for latitude j (this number will depend on j only for reduced Gaussian grids), and w_j is the Gaussian weight for latitude j. These weights are normalized such that their sum over all latitudes is unity.

The first step in the evaluation of the P_{ij} requires the spectral transformation from C to B_{ij} and $(D_u, D_v)_{ij}$. The next step is the evaluation of $F(\lambda', \theta')$. Following Ritchie (1987 [18]), we define latitude-longitude points in terms of 3–dimensional cartesian vectors centered on the unit sphere. The origin point (λ', θ'), corresponding to the 3–dimensional cartesian vector $\boldsymbol{r}$, is then found in the plane of the endpoint location vector $\boldsymbol{g}$ (corresponding to gridpoint (λ_i, θ_j)), and the displacement vector $\boldsymbol{d}$ (corresponding to $(D_u, D_v)_{ij}$):

$$\boldsymbol{r} = \alpha \boldsymbol{g} + \beta \boldsymbol{d},$$

where the coefficients α and β are chosen to satisfy the constraint that $\boldsymbol{r}$ must lie on the surface of the sphere, and that the length of the displacement vector $\boldsymbol{d}$ is equal to the great circle distance between $\boldsymbol{g}$ and $\boldsymbol{r}$. Finally, the value $F(\lambda', \theta')$ is obtained by bilinear interpolation in longitude and latitude from the surrounding grid point values.

3.2 Smoothness penalty function, J_d

The smoothness penalty function, J_d is given by a simple quadratic form in terms of the spectral coefficients of the distortion,

$$J_d = \Sigma_j w_j (C_j - \tilde{C}_j)^2, \tag{1}$$

where j ranges over the ordering of the spectral wavenumber vectors, k, and over the components of the distortion—B, ζ, δ. The $\tilde{C}$ are the background or first guess of the distortion.

Thus it is the increments of C which are constrained. A reasonable first guess is the estimate of C obtained for the same forecast, but valid 6 or 12 h earlier. This is a method to enforce consistency in the evolution of the distortion. Consistency is most lacking if a feature in the forecast may be explained in terms of more than one feature in the verification. These situations are more likely to occur as forecast length increases. Different specifications of w_j are possible. For example, consider the part of J_d due to the bias correction. In continuous form this is given by,

$$J_{d,B} = \frac{1}{\sigma_B^2} \int \int (\nabla^{2\nu}[B - \tilde{B}])^2.$$

Here ν is an adjustable parameter normally taken to be 1 and σ_B is the scale for B. Larger values of ν result in greater smoothing by emphasizing the contributions of higher wavenumbers to J_d. Using the spectral representation of B, the orthonormality of the spherical harmonics ${\Psi_n}^m$, and the eigenstructure $\nabla^2 {\Psi_n}^m = -n(n+1){\Psi_n}^m$, we find that,

$$w_{k,B} = (n_k(n_k+1))^{2\nu}/\sigma_B^2.$$

3.3 Barrier penalty function, J_a

The functional J_a serves to limit the amplitude of the distortion. For efficiency the limits are set on the spectral coefficients. These limits are chosen in such a way that the grid point (or physical space) values of bias and displacement at all locations will be limited by specified values. In addition the spectral coefficient limits provide a good scaling (or conditioning) for the minimization. Test runs using synthetic data indicate that convergence of the minimization is sensitive to the scaling of the control vector.

The form of J_a is chosen to be,

$$J_a = \Sigma_j([C_j - \tilde{C}_j]/S_j)^{2\mu},$$

where S_j are the spectral limiting values for the increment of C_j. The adjustable parameter μ, nominally 10, controls the steepness of the barrier in spectral space (Fig. 1).

There is no unique way of setting the spectral limits. We choose limits which correspond to an equipartitioning, among the spectral modes, of the contributions to the physical space bias correction or displacement component. Here mode means each pair (m, n). The reasoning for this is that no matter what the signs of the spectral coefficients, the modes will tend to add up somewhere in the physical domain. On the other hand, the contributions within a particular mode, for example due to the sine and cosine components, are always out of phase and therefore add up in an *rms* sense. The limits on components are chosen to correspond to a further equipartitioning.

3.4 Implementation details

The algorithm is implemented in Splus and Fortran. The spectral transform and computation of Gaussian latitudes and weights use a set of general purpose Fortran library functions. All

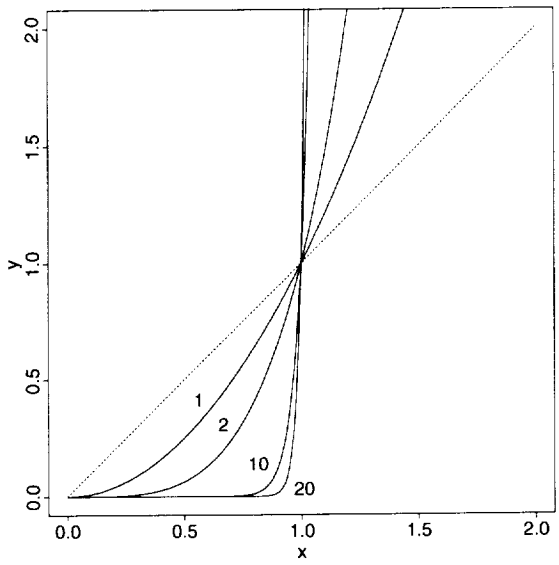

Figure 1: The component of the barrier function for a single term ($y = x^{2\mu}$ where $x = C_j/S_j$), for μ equal to 1, 2, 10, 20.

computations are performed in double precision. To minimize J we use the built-in Splus function `nlminb`, which implements the algorithms of Dennis *et al.* (1981 [3]). The `nlminb` algorithm uses function and gradient values. Second derivatives of the cost function are estimated by finite differences, using repeated evaluations of the gradient and cost function.

At first we used the version of the minimization algorithm which requires function values only. However, the finite difference approach is computationally inefficient, and we have recently developed the adjoint of the calculation of J. To develop the adjoint we use tools previously developed for this purpose (Hoffman *et al.* 1992 [8]). In addition, in the present case the spectral transforms are nearly self-adjoint (Hoffman and Nehrkorn 1989 [9]), so the amount of actual adjoint code for the transforms is limited. The adjoint calculates the gradient of the cost function very efficiently. This technique gains more than an order of magnitude decrease in computational time and provides a more accurate gradient. The efficiency of the adjoint code allows us to use more than enough iterates. All results presented here use 100 iterations.

The minimization starts from the reasonable initial estimate of zero distortion. This is a point of maximum non-differentiability. To eliminate this problem, we interpolate the original analysis to a new grid using Gaussian latitudes and longitudes offset by half a grid length. Now a zero displacement corresponds to locations interior to the grid of the analysis, where the interpolation of the analysis is differentiable.

4 Results

Results obtained from our method during this past year extend the results reported previously to additional variables, forecasts, and truncation parameters of the distortion. Sensitivity tests involving different choices of truncation parameters are described in Section 5.2. We report here on the results of distortion experiments for isentropic potential vorticity (IPV), concentrating on the 315 K isentropic surface (q315), and compare those with results for the 500 hPa geopotential height (h500) and sea level pressure (slp). We have computed distortions for all three variables, for the CONTROL forecast started at 00 UTC 11 March 1993, for forecasts from 12 to 120 hours, every 12 hours. This forecast period includes the so-called "Superstorm 93", an exceptionally intense cyclone on the East Coast of the United States. Truncation sensitivity tests were also performed for the CONTROL forecast started at 00 UTC 6 March 1993 (see Section 5.2).

A summary of the minimization results is shown in Table 1, which shows the statistics of the minimization.

Table 1: Summary statistics for 315 K IPV (q315), 500 hPa height (h500), and sea level pressure (slp) for the CONTROL forecast every 12 h.

	slp			h500			q315		
Forecast	Rms Error		Var.	Rms Error		Var.	Rms Error		Var.
Hour	Initial	Final	Expl.	Initial	Final	Expl.	Initial	Final	Expl.
012	1.495	0.761	74.1	20.323	8.309	83.3	0.296	0.227	41.1
024	2.383	1.049	80.6	26.775	10.298	85.2	0.375	0.271	47.8
036	3.549	1.521	81.6	33.514	11.247	88.7	0.465	0.331	49.3
048	4.903	1.993	83.5	42.399	13.494	89.9	0.601	0.362	63.7
060	6.005	2.084	88.0	51.822	15.881	90.6	0.664	0.378	67.6
072	6.627	2.247	88.5	62.590	14.795	94.4	0.770	0.414	71.1
084	7.473	2.298	90.5	73.342	17.407	94.4	0.862	0.417	76.5
096	8.577	2.296	92.8	86.126	21.365	93.8	0.933	0.445	77.2
108	9.748	2.436	93.8	103.189	24.016	94.6	0.965	0.483	75.0
120	11.176	2.512	94.9	118.070	27.080	94.7	1.021	0.504	75.6

In Table 1 the rms error is the rms residual error for the hemisphere (in m, hPa, and PV units, respectively), calculated as the square root of J_r. Initial values are for a zero distortion, final values for the solution. The last column is the fraction of the initial error variance (J_r) explained by the distortion (in %).

In the reported cases 100 iterations were used by the minimization, and we took $\tilde{C} = 0$. The distortions all used a triangular truncation at wavenumber 10 (T10), and computations were restricted to the Northern Hemisphere. Potential vorticity forecast fields were found to be excessively noisy near the poles, so we applied a smoother to both the forecast and verification fields north of 70°N.

Clearly the minimization greatly reduces the size of the residual error, more so for longer forecast periods, and most for the h500 field, less so for the slp field, and least for q315. The reason for this is that the distortions are limited to large scales, and the forecast errors at short forecast lengths, and for the q315 and slp variables, have more energy at smaller scales. For a qualitative assessment of the results, we turn to the forecasts of the Superstorm 93.

4.1 Superstorm 93

The 60 h forecast valid at 12 UTC 13 March 1993, shown alongside the verifying fields in Fig. 2, is at the early stage of the Superstorm 93 development. Both phase and amplitude errors are clearly apparent in the sea level pressure field: the center of the low is too far to the westnorthwest, and about 30 hPa less deep than in the verifying analysis. At 500 hPa, the height field shows similar errors: the trough is not as deep and not as far east as in the analysis. The 315 K IPV field shows a southward extrusion of high IPV, which is too broad and weak in the forecast. The distortions applied to these forecasts (Fig. 3) all correct the errors to some degree, and they are generally consistent with each other, even though there are differences in the details. In particular, the slp corrections of the cyclone have a large bias correction, whereas the height and especially the IPV distortions rely more on displacements. As Fig. 4 shows, the original forecast errors contains more energy at the small scales for the IPV field, but the large-scale distortions (using the T10 truncation) manage to remove a large part of these errors.

At the mature stage of development (84 hours into the forecast), the forecast captures the intensity of the storm, but the position of the surface low is too far to the southwest (Fig. 5). At 500 hPa the verification has an intense trough to the northeast of a secondary trough, whereas the forecast has a cutoff low in the position of the secondary trough. The IPV extrusion is not as wrapped around and as far to the northeast in the forecast as in the analysis. The distortions in this case (Fig. 6) all have northeastward displacements, and a pattern of bias corrections that act to weaken the surface low, and strengthen the upper level vorticity (and lower the heights and pressures) to the west.

One of the motivations for considering the IPV field was the fact that it is a quasi-conserved quantity. We investigated whether the distortions applied to this field would be less ambiguous, and exhibit more time continuity, than those applied to the height and pressure fields. For the cases examined so far, this holds true. An example of this is shown in the time series of IPV distortions for the Superstorm 93 case (Fig. 7).

5 Covariances for background penalty terms

We have developed an approach to determine statistics of the distortion from available data.

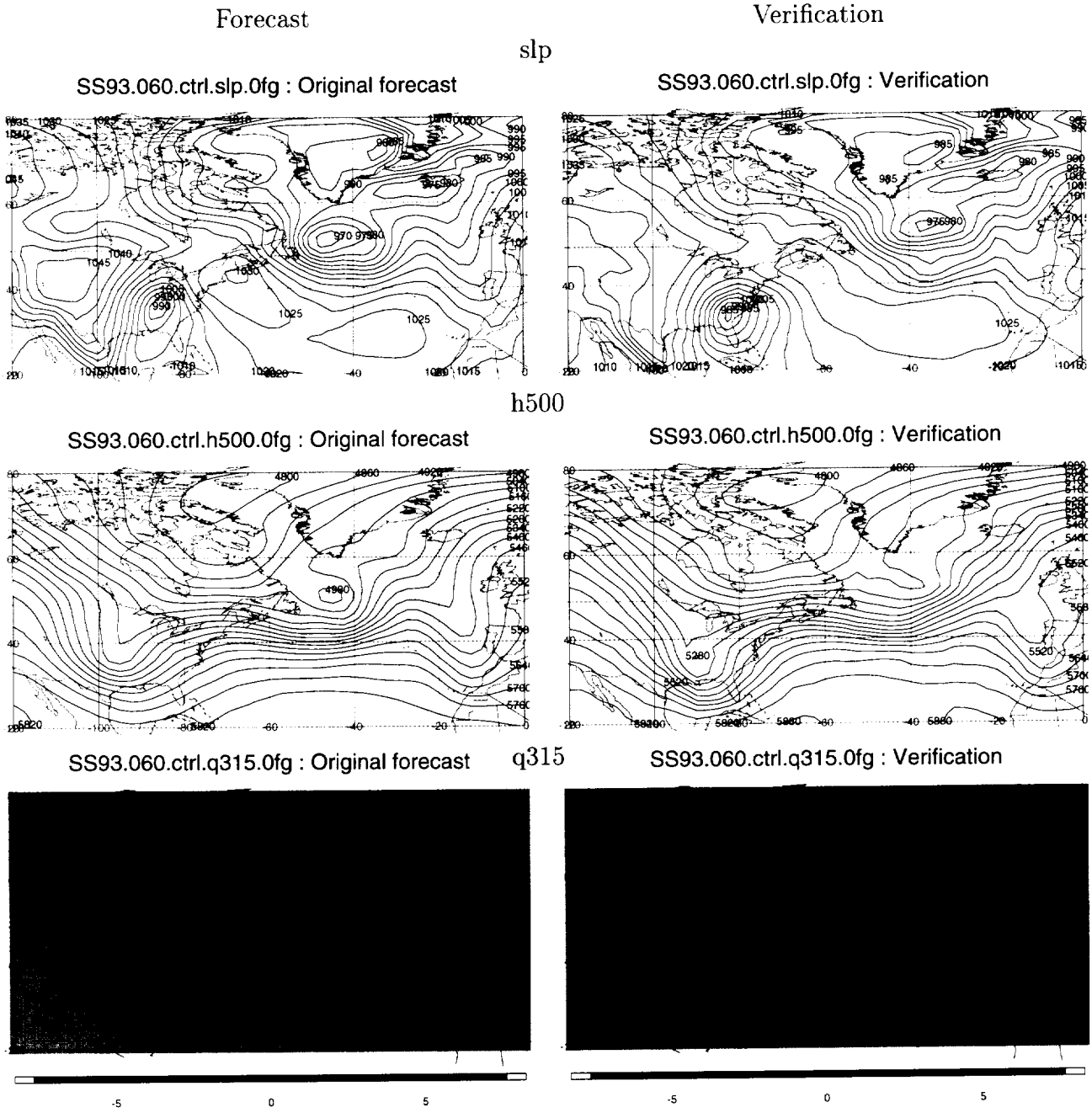

Figure 2: CONTROL forecasts at 60 h and verifying fields for the Superstorm 93 case.

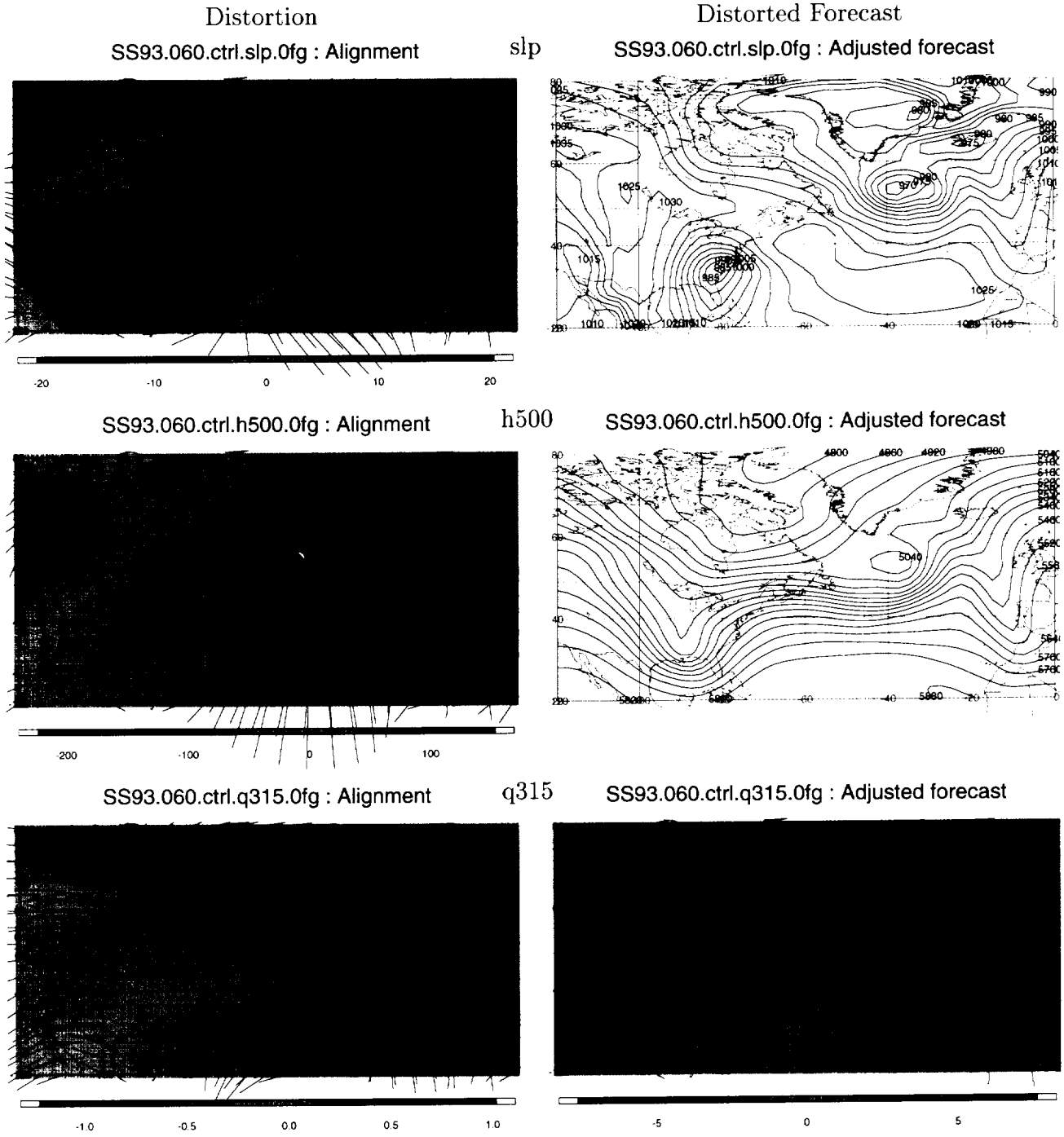

Figure 3: Distortions and distorted forecasts at 60 h for the Superstorm 93 case.

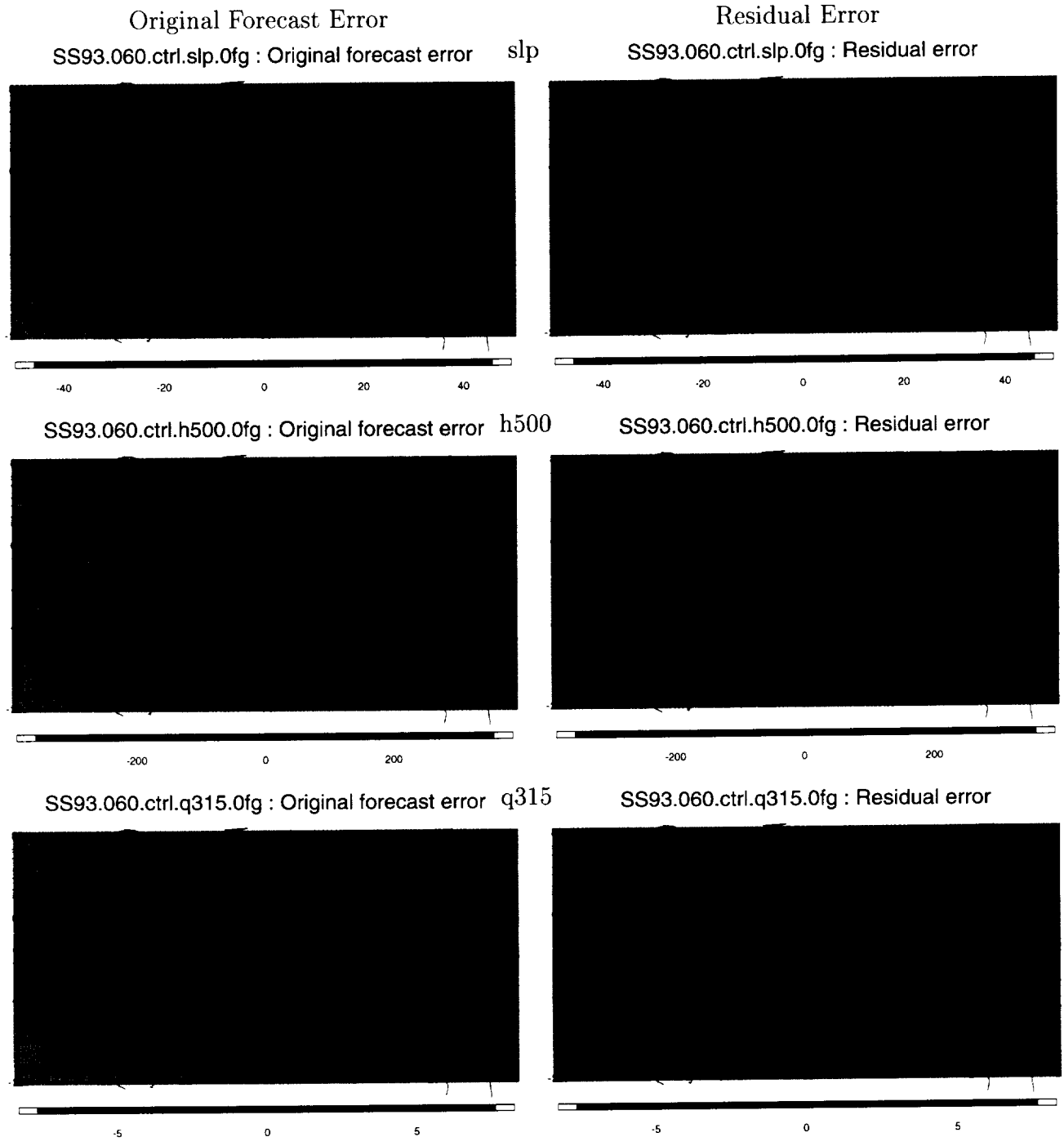

Figure 4: Original forecast and residual errors for forecasts at 60 h for the Superstorm 93 case.

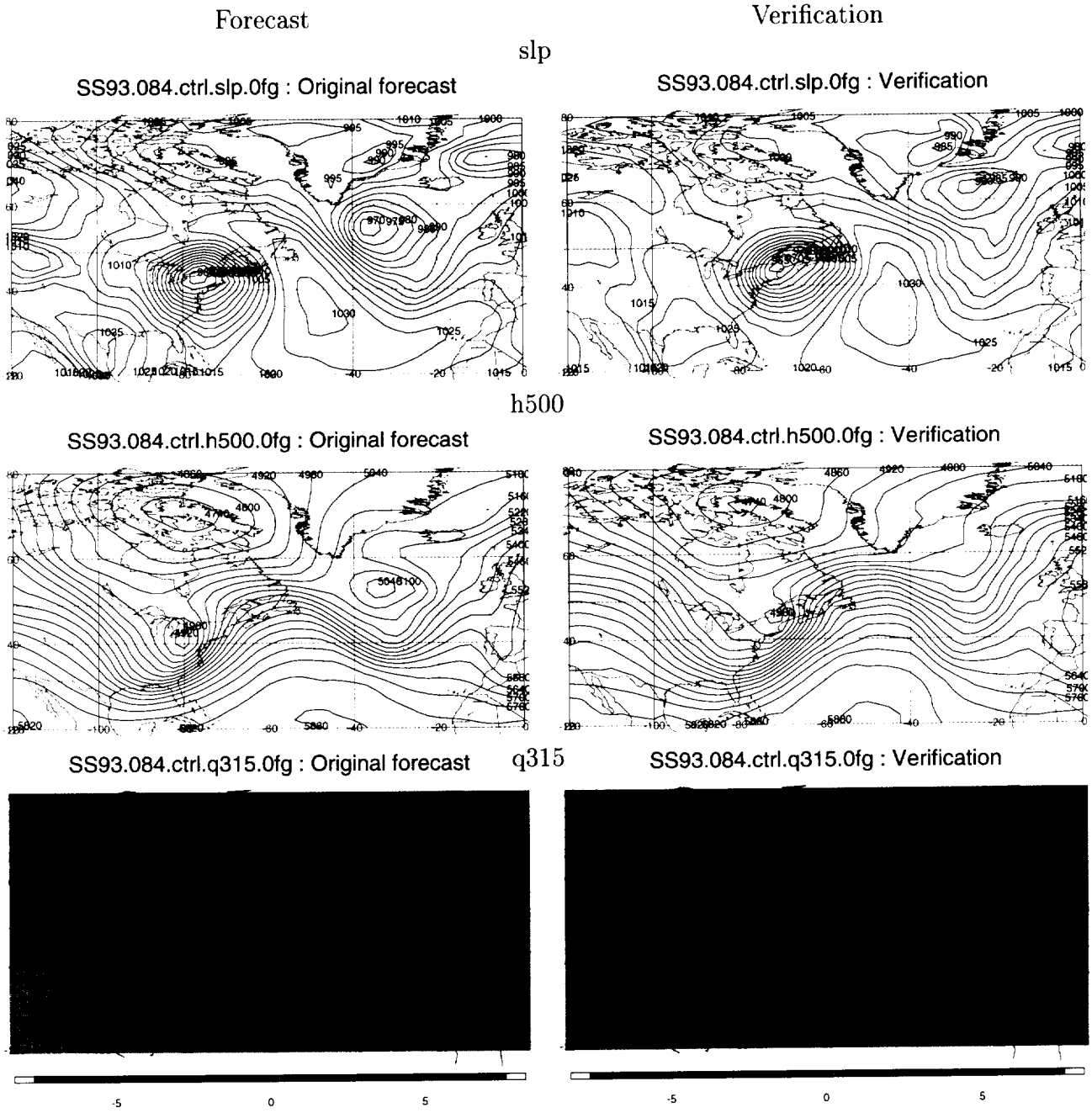

Figure 5: CONTROL forecasts at 84 *h* and verifying fields for the Superstorm 93 case.

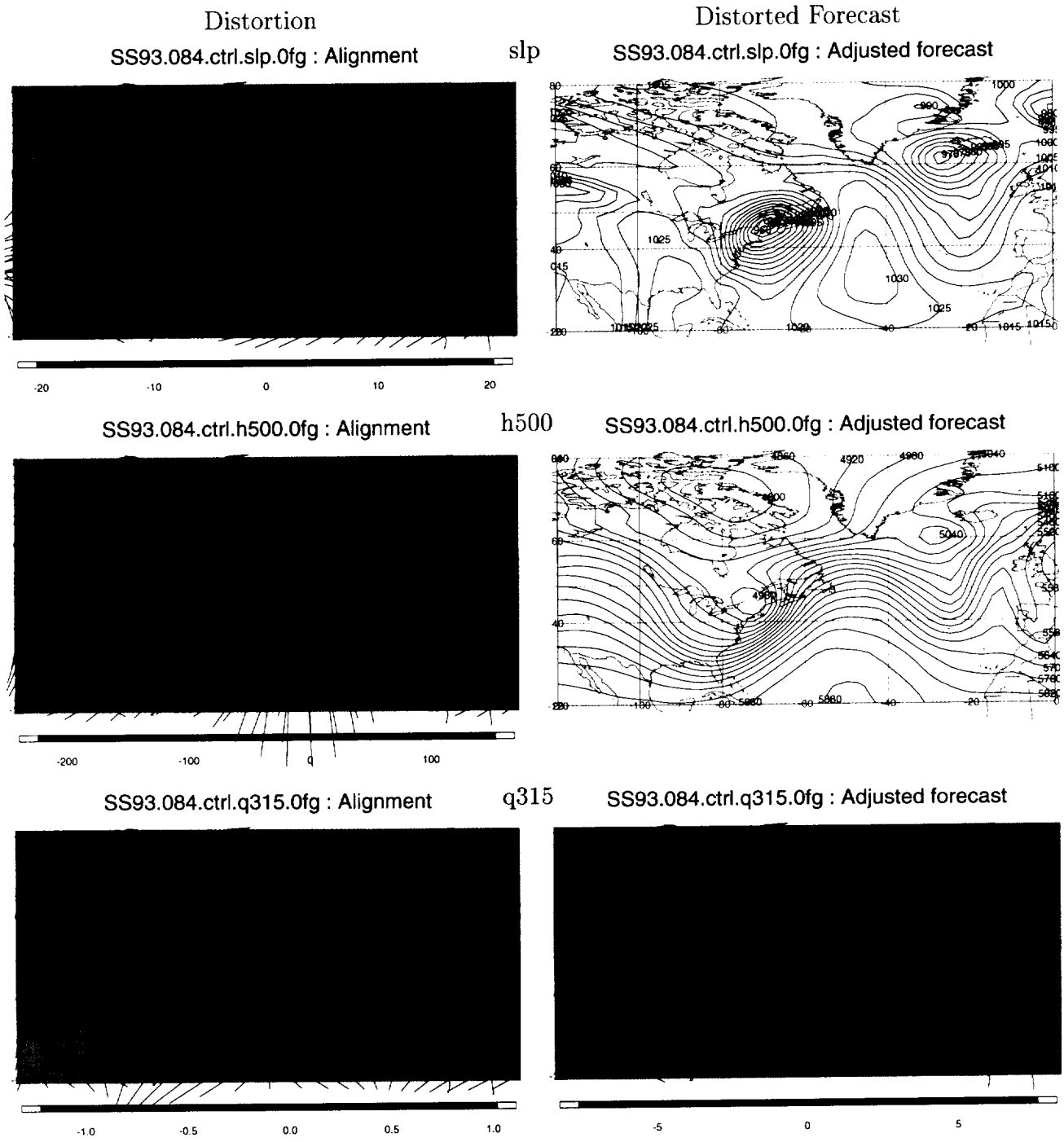

Figure 6: Distortions and distorted forecasts at 84 h for the Superstorm 93 case.

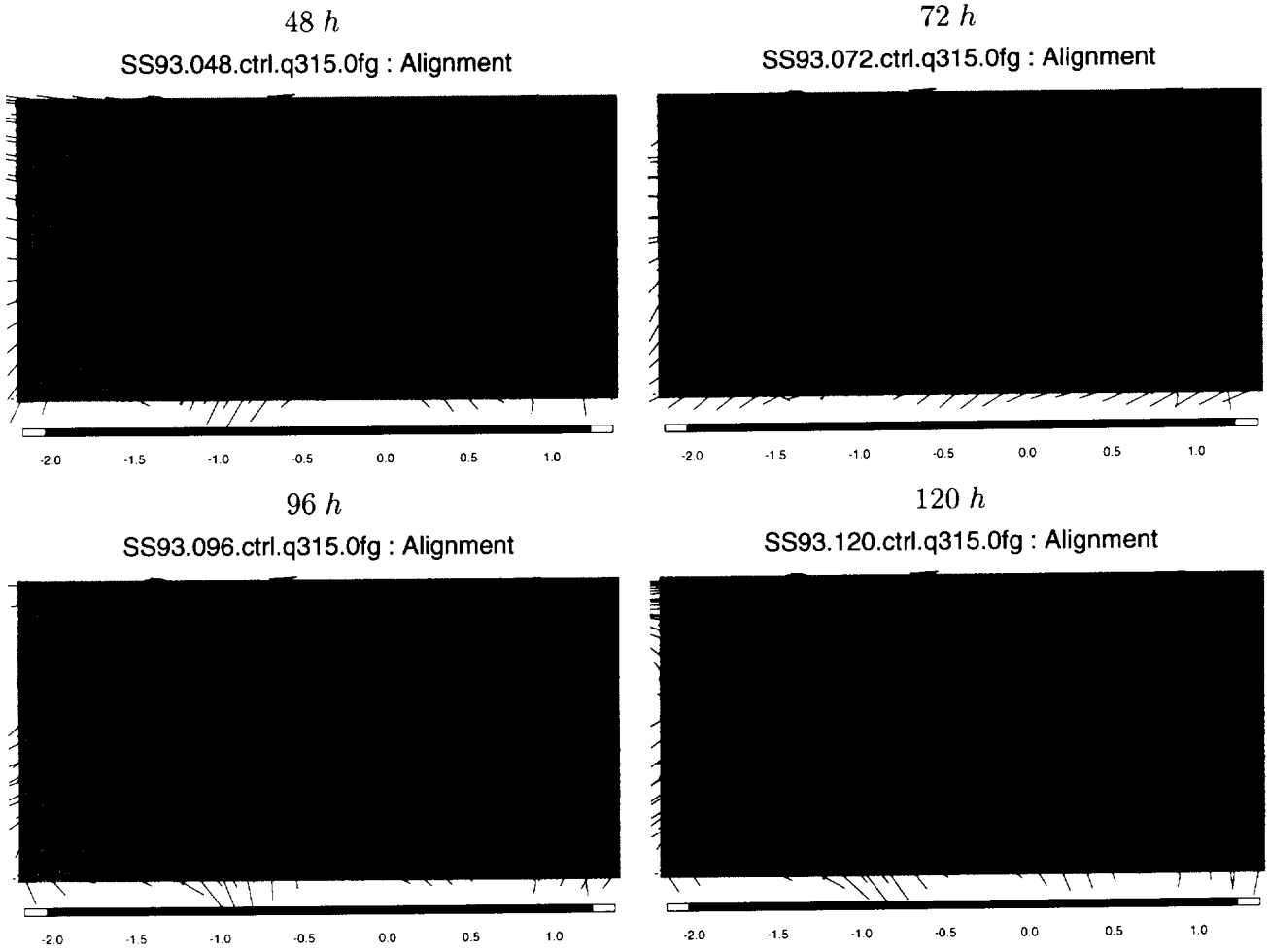

Figure 7: Distortions at 48 h–120 h for the Superstorm 93 case.

5.1 Methodology

Parish and Derber (1992 [13]) and Parish *et al.* (1997 [14]) (in the JMSJ special issue), use a small (30–45) sample of cases of forecast divergences to develop all the statistics needed for the background and balance constraints. The forecast divergences are $48 - 24$ h forecast differences for forecasts verifying at the same time. An empirical rescaling gives the 6 h forecast errors. This so-called "NMC" approach, has also been used successfully at ECMWF. At ECMWF the empirical rescaling factor was found to be 0.9 by comparing TOVS radiance data to the 6 h forecast (Rabier *et al.* 1997 [15]).

Using alignments to represent the forecast errors separates J_b, the background penalty functional into J_r, the residual penalty term measuring the misfit between the aligned background and the analysis and J_d measuring the size of the alignment. Both of these are quadratic terms. J_r is analogous to J_b and would be formulated in terms of the same analysis variables.

The key assumptions about the forecast errors made in the NMC method are

1. That the physical analysis variables chosen—vorticity, divergence, specific humidity, unbalanced temperature and unbalanced log of surface pressure—are uncorrelated.

2. That the individual spherical harmonics (or the spherical harmonics for different total wavenumber n) are uncorrelated.

3. That for each analysis variable, a vertical correlation function may be specified either globally or for each total wavenumber n.

As a result of these assumptions, to calculate J_b, the model state is transformed to analysis variables, analyzed into spherical harmonics, and projected on the vertical EOFs of the vertical covariance matrices. The EOF coefficients are then squared and weighted by their inverse variances, which are the eigenvalues of the associated EOFs.

Given a formulation of J_d the NMC approach could be used to derive the covariances for J_r. We would use J_d to calculate an alignment for each forecast divergence. Then the residual differences would be analyzed by the NMC method. Our problem is to define the covariances for J_d.

Here is a a possible approach, similar in flavor to the NMC approach.

1. Convert forecasts to variables to be aligned on the appropriate iso-surfaces. For example, potential vorticity on constant potential temperature surfaces. Initially we examine 500 hPa data only.

2. For each case, for each alignment variable at each level calculate an alignment without constraints, by using a form of J_r based on a simple energy norm. Use no constraints, but use a forward stepwise approach to determine the spectral truncation. Initially use a $T10$ truncation. Increase the truncation in steps, stopping when the increase in the fraction of explained variance per degree of freedom added is less than some critical value (say 1%). The largest wavenumber retained will vary from case to case. Save

the alignment for subsequent analysis. If the alignment is saved in spectral space, be sure to include zero values for all wavenumbers greater than the largest wave number retained. Initially we examine only displacements.

3. Develop a global vertical covariance matrix or vertical covariance matrices for each n, for each alignment variable from the sample of alignments. For quality control, these covariances should be based on trimmed samples. That is, for each alignment variable at each level, set the extreme values to zero. Either a critical fraction (say 3%) would be considered extreme, or the extreme values could be determined so that the trimmed sample is close to a normal distribution.

4. The specification of J_d is now complete. It should be applied to the original sample as a consistency check. The alignments found with J_d should be similar to those found in the previous calculation of adjustments, except for cases when extreme values were trimmed. The residuals resulting from applying J_d can now be analyzed to obtain the specification of J_r.

5. As a second consistency check, calculate the alignments with the current esimates of J_r and J_d. If the results are not substantially the same as before, go back to step 3.

5.2 The stopping criterion

Determining the stopping criterion for adding degrees of freedom to the representation is critical. There are different ways of adding degrees of freedom to the distortion. In the results described so far, we have used the bias correction, and rotational and divergent displacements in the distortion representation, using the same T10 truncation for all 3 components. In the following, we describe experiments in which we use one (rotational displacements), two (rotational and divergent displacements), and all three components, using a range of truncation wavenumbers in each case. We have examined the results of these tests, using an analysis of variance approach (using an f-test stopping criterion), and an examination of the statistical properties of the residual error field (in particular, to what extent the correlation structure is homogeneous and isotropic).

5.2.1 Analysis of Variance

To determine a stopping criterion based on an analysis of variance, we consider the reduction in the residual error variance as a result of increasing the spectral truncation of the distortion representation. The f-statistic we compute is given by:

$$F^* = \frac{(SSE(n_2) - SSE(n_1))/(df(n_2) - df(n_1))}{SSE(n_2)/(N - df(n_2) - 1)} \quad ,$$

where F^* is the f-statistic corresponding to an increase of the spectral truncation from n_1 to n_2, $SSE(n)$ is the residual error variance for truncation wavenumber n, $df(n)$ is the number

of degrees of freedom in the corresponding distortion representation. As an estimate of the degrees of freedom associated with the total error field (N) we use the degrees of freedom contained in the spectral representation of the error field, for a rhomboidal truncation sufficient to reproduce the gridded field on the Gaussian grid used during the minimization (for the hemispheric fields used in these experiments, $N = 1277$).

For a given truncation wavenumber n_1, increasing the distortion truncation to n_2 results in a significant reduction in residual error variance if

$$F^* > F(p; df(n_2) - df(n_1), N - df(n_2) - 1) \ ,$$

for the significance level p.

For the potential vorticity field, we have computed the significance level of the above f-test for three separate cases: "default" (using all three distortion components), "noamp" (using only displacements), and "nodiv" (using only nondivergent displacements). In the latter case, the hemispheric mean IPV is conserved during the distortion, corresponding to a purely adiabatic redistribution of the original PV. For the height and pressure field, we only considered the "default" and "noamp" cases. In each case, the truncation of the distortion is a triangular truncation, and the f-test is applied to $n_2 = n_1 + 3$, i.e. for the case when the truncation wavenumber is increased by 3. The degrees of freedom contained in the distortion for the three cases is shown in Fig. 8.

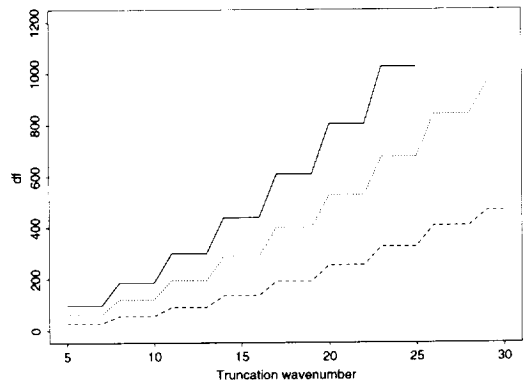

Figure 8: Degrees of freedom in the distortion, as a function of triangular truncation wavenumber (from T5 to T30, in increments of 3), for the hemispheric distortion for "default" (solid line), "noamp" (dotted), and "nodiv" (dashed).

A summary of the results for the hemispheric 12-hour and 96-hour forecasts in the Superstorm 93 case is shown in Fig. 9. Results are shown for the q315, h500, and slp fields, for truncation wavenumbers between T5 and T25 (T30 for the "nodiv" case). The monotonically increasing lines show the fraction of the explained variance as a function of the degrees of freedom in the distortion representation. For a given truncation, they are always highest for h500, and lowest for q315, as discussed above. It is interesting to note that, at

12 hours, the "default" representation results in the lowest residual error compared to the other representations with the same degrees of freedom, for all three fields. However, at 96 hours, the "noamp" distortion (using displacements only) is more efficient for distorting the q315 field. The significance level p is unity or close to it for low truncations, but generally drops below 0.95 at some truncation below the maximum considered in these experiments. The critical truncation wavenumber depends on the type of distortion, the forecast field, and the forecast hour.

We have repeated these computations for the other forecast hours, and for the other CONTROL forecast (initialized at 00 UTC 6 March 1993), with generally similar results.

5.2.2 Residual error correlation structure

One of the justifications for using FCA is that the residual forecast errors are likely to be more homogeneous and isotropic than the original forecast errors. Visual comparison the original and residual error fields (Fig. 10) appear to support this hypothesis. However, the main difference between the two fields is the scale of variability: the residual errors have a much smaller scale than the original errors. This is forced by the FCA method, which projects the large scale errors onto the adjustment field. To test the hypothesis of homogeneity and isotropy of the residual errors, we computed and compared the error correlations of the original and residual errors, for several forecasts, at several lead times and with several truncations of the adjustment field.

As before, we considered the 500 hPa height, the surface pressure and the potential vorticity on the 315 K potential temperature surface. The adjustment fields were computed by minimizing the difference between the forecast and the corresponding analysis. It was done independently for the three variables, so that the adjustment field for the 500 hPa height is not the same as that for the surface pressure or the potential vorticity.

Since this work is part of the study to determine the optimum truncation in defining the adjustment field, we used truncations from T05 (triangular truncation with 5 waves around the equator) to T25.

We first examine the 500 hPa height fields. We have the data on a regular latitude–longitude grid. We divide the zero to sixty degrees latitude zone into twelve equal size regions, sixty degrees of longitude by thirty degrees of latitude. We ignore the polar region to avoid having to deal with the convergence of the meridians. Within each region we compute the error correlation in eight different directions and at separations of 2 to 10 degrees of great circle distance. To examine the homogeneity of the error fields, we average the correlations over all the angles within each area. Figures 11 and 12 show these correlations for forecast starting on two different days: 6 March 1993 and 11 March 1993.

It can be seen from these two figures that the residual forecast error correlations behave in a systematic fashion as the truncation of the distortion field increases. At very low truncation the adjustment process cannot account for much of the forecast error and the residual errors are correlated at long distances, in a way not too dissimilar from the forecast error correlations. This correlation scale decreases as the truncation of the displacement

12 h

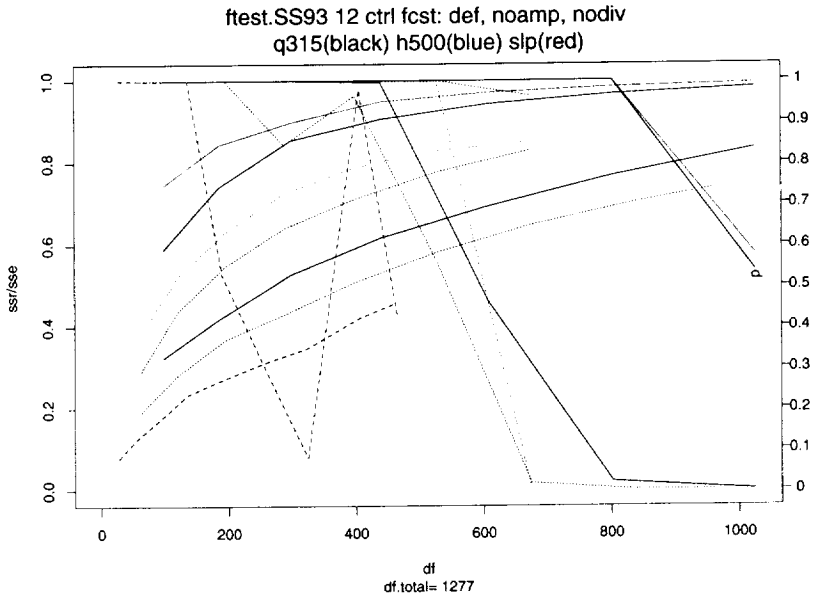

96 h

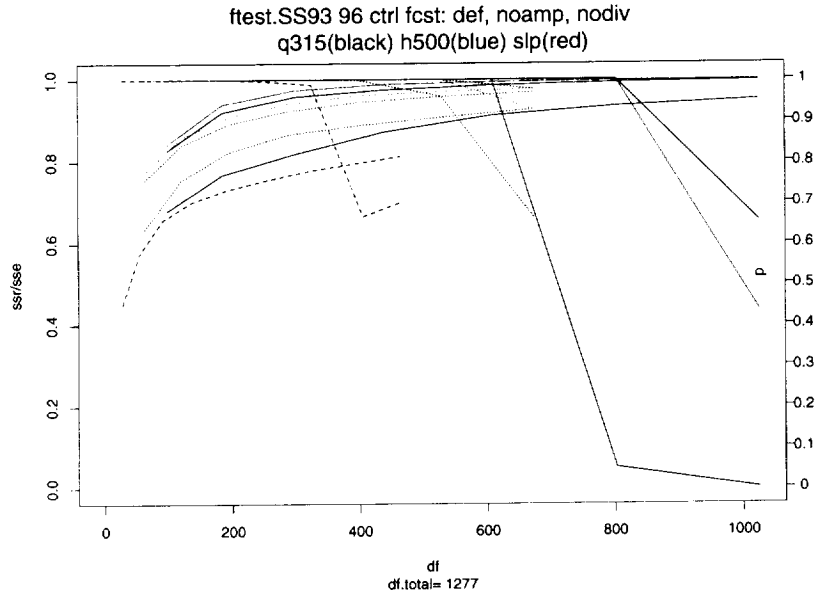

Figure 9: Summary plot of the distortion ftest for 12 h (top) and 96 h (bottom) Superstorm 93 forecasts. Results are shown for the q315 (black), slp (red), and h500 (blue) fields, as a function of the degrees of freedom retained in the distortion representation. Solid lines are for the "default" case, dotted for "noamp", and dashed for "nodiv". Shown are the fraction of explained variance, and the p-values of the f-test.

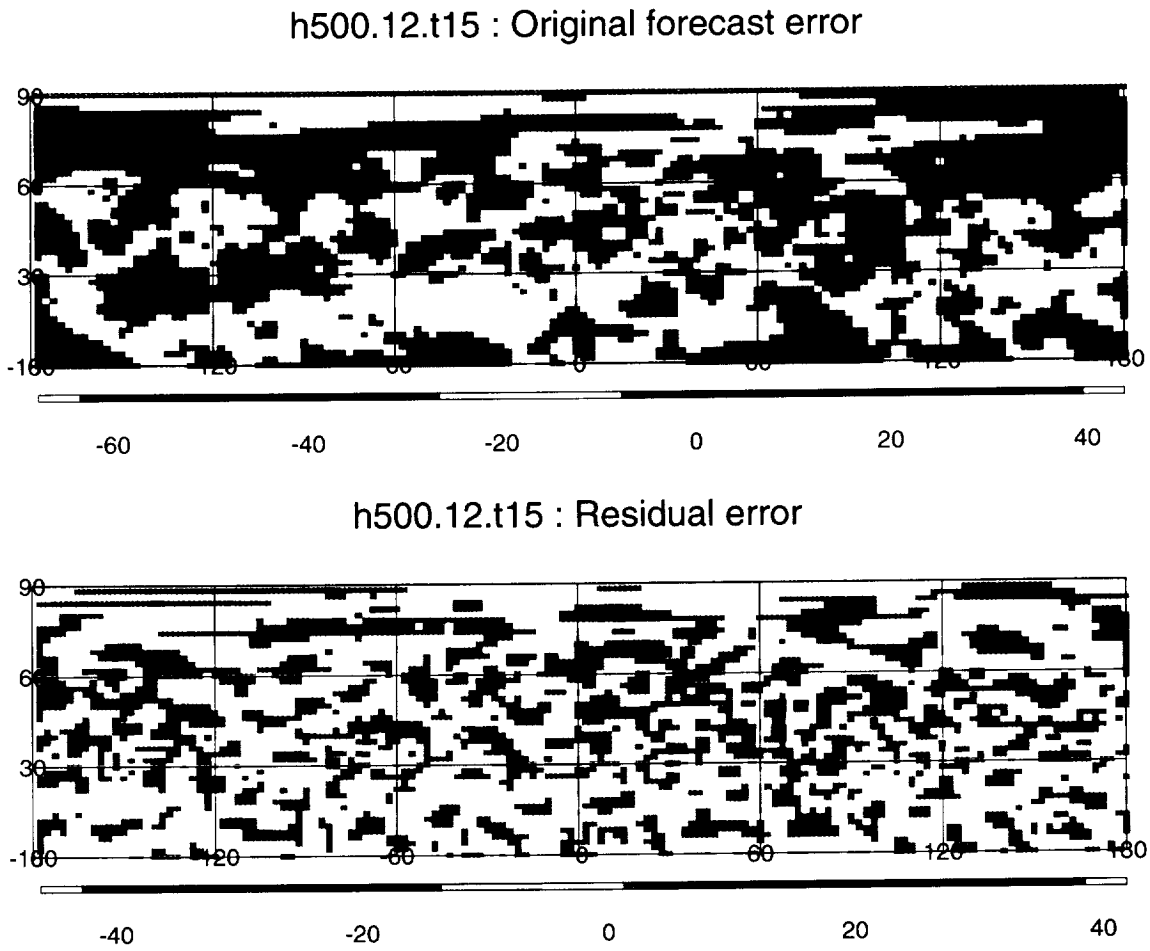

Figure 10: Original and residual 12 hour forecast error of 500 mb height on 11 March 1993. Displacements are computed with T15 truncation.

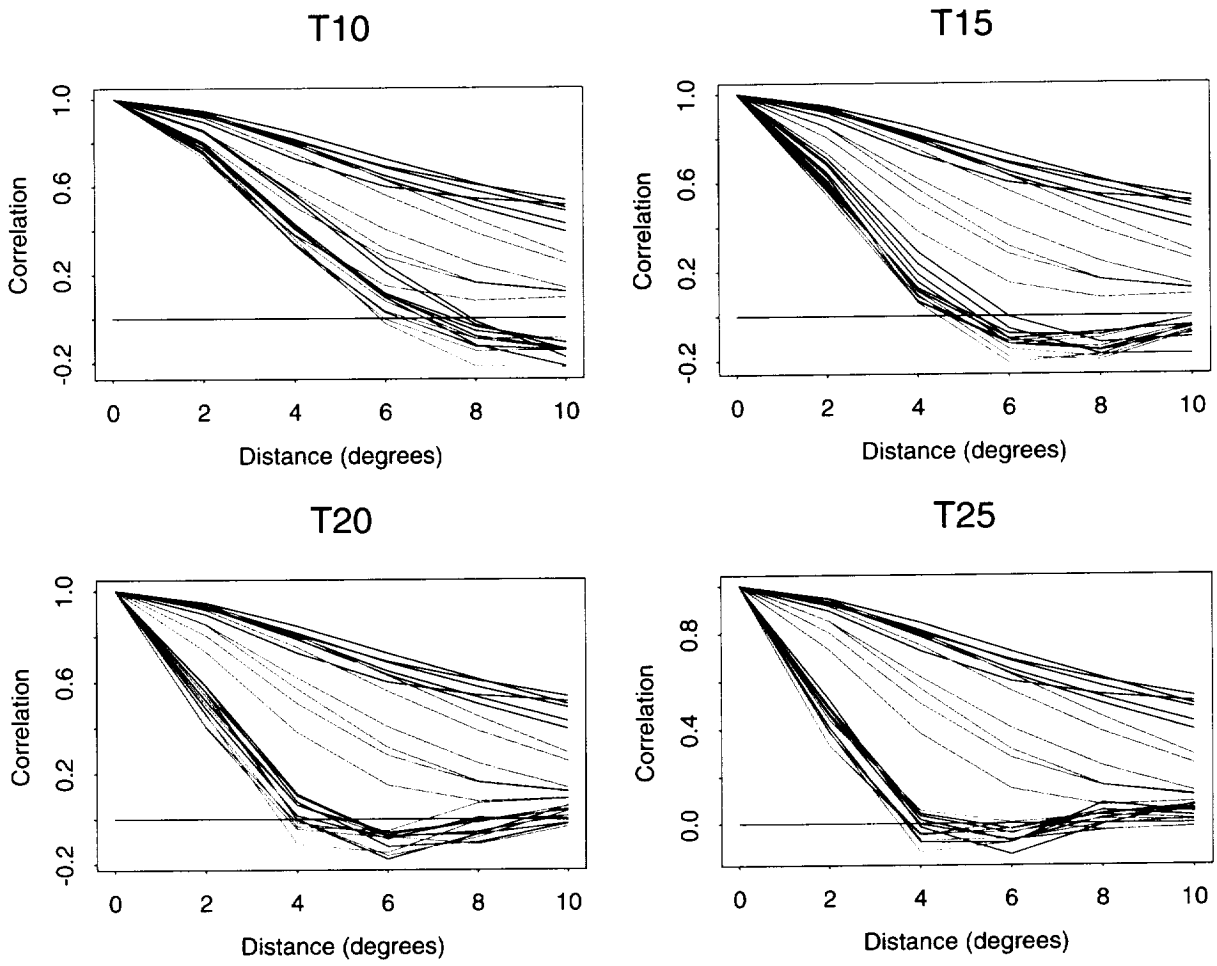

Figure 11: Error correlations averaged over all angles, in each of the 12 areas. Each plot shows the original error correlations in black (tropical areas) and blue (extratropical areas) and the residual error correlations in magenta (tropics) and green (extratropics) when the adjustment are computed with the indicated truncations. Twelve hour forecast from 6 March 1993.

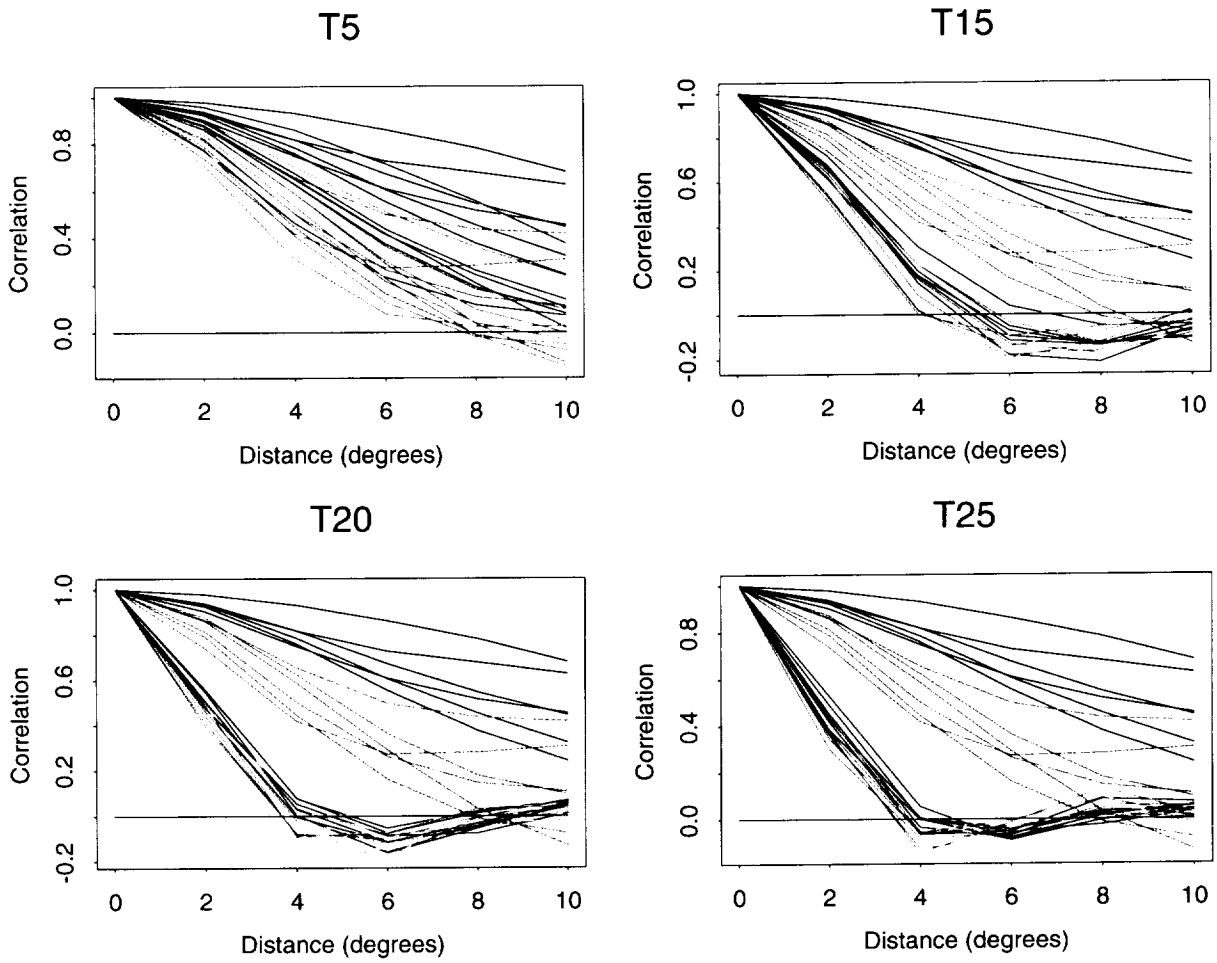

Figure 12: Same as Fig. 11 but for forecast from 11 March 1993

field increases, but little difference can be seen between the T20 and T25 truncations. At the same time the curves for the different regions become much more similar. This indicates that, beyond truncation T20 or so, the residual error correlations are much more homgeneous than the original forecast error correlations. It can be noticed that a large part of the inhomogeneity in the original error correlations is due to a large difference between the tropical and extra-tropical regions. This difference also appears in the residual errors, but to a much lesser extent.

To evaluate the isotropy of the error correlations, we computed the correlations in eight different directions, every 22.5°. Figure 13 shows the spread of these curves for the original forecast errors and the T25 residual errors, for the 6 March 1993 forecast. The mean curves are averaged over all areas and all directions. The standard deviation with respect to the different directions is computed separately in each area, then averaged and added to or subtracted from the mean curve to obtain Fig. 13. It is clear that the residual error is much more isotropic than the original error. The figure for 11 March 1993 (not shown) is almost identical.

6 Plans for future work

A great deal of novel work has been accomplished under the current contract. In broad terms we have developed and tested an efficient algorithm for determining distortions. The algorithm and constraints are now ready for application to larger data sets, to be used to determine the statistics of the distortion as outlined above, and to be applied in data analysis by using GOES water vapor imagery to correct short term forecast errors. This future work is described in more detail below. A proposal (AER P778) to continue this work has been approved by NASA HQ in November of 1997 (UPN 622-242621), but is still under negotiation between AER and GSFC. An announcement of GSFC's intent to issue a Request for Offer (RFO)5-60741-253 to AER was made in CBD on 7 August 1998.

6.1 Use of the 6.7 μm water vapor imagery

The second set of our proposed experiments compare satellite data—in this case geostationary 6.7 μm water vapor imagery—to a background field calculated from a short term forecast. The 6.7 μm water vapor imagery data are ideal for our study since they have striking patterns and features, which can be matched by corresponding patterns and features in the short term forecast. Additionally geostationary water vapor data are available with high temporal frequency and near global coverage. However, we will begin our investigation with GOES data only, since the METEOSAT sensors do not have on-board calibration. (See Schmetz and Turpeinen (1988 [19]) for a discussion of the calibration of these data.)

The approach for this task will be similar to that taken for the 500 hPa height fields. In this case, we take the short term forecast of the 6.7 μm water vapor imagery as X_f and the observed imagery as X_a. There are two complications: the calculation of the simulated 6.7 μm water vapor imagery, which is discussed in the next paragraph, and the need to quality

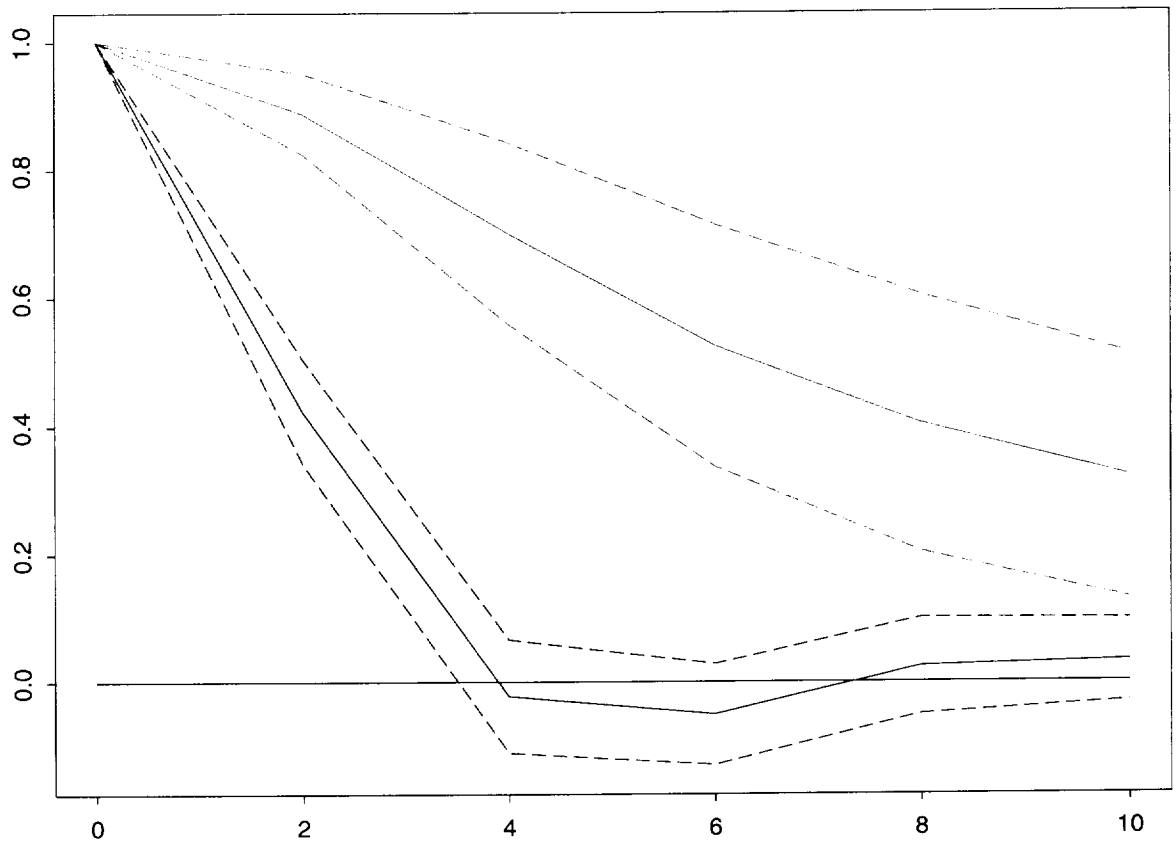

Figure 13: Mean correlation curve and mean +/- one standard deviation for original forecast errors (blue) and T25 residual errors (magenta). Forecast from 6 March 1993.

control the observed imagery. Quality control is required because of limited coverage, missing data, and the difficulty of simulating the 6.7 μm water vapor imagery at large incidence angles, over high terrain for dry conditions, and in the presence of cloud. It will be necessary, at least initially, to resample the imagery to a relatively coarse resolution. Then we will determine smooth displacement and amplification fields needed to best match the forecast and imagery. The algorithm needed here is identical to that used for the 500 hPa height fields. The resulting field of displacement provide a correction to the short term forecast.

We will simulate the 6.7 μm water vapor imagery from the forecast values of temperature and humidity using a standard radiative tranfer model (RTM). The simulated 6.7 μm water vapor imagery will then be held fixed in determining the distortion. Changes in incidence angle related to displacements on scales of 100 km are $O(1°)$. The sensitivity of the calculated brightness temperature to incidence angle is small (Fig. 14) and will be assumed negligible in these calculations. The RTM used in Fig. 14 is MODTRAN (Berk *et al.* 1989 [2]). (MODTRAN is not efficient; our candidate for future calculations is OPTRAN (McMillin *et al.* 1995 [11]). During the past year we have obtained and tested OPTRAN, using a standard set of atmospheric profiles.)

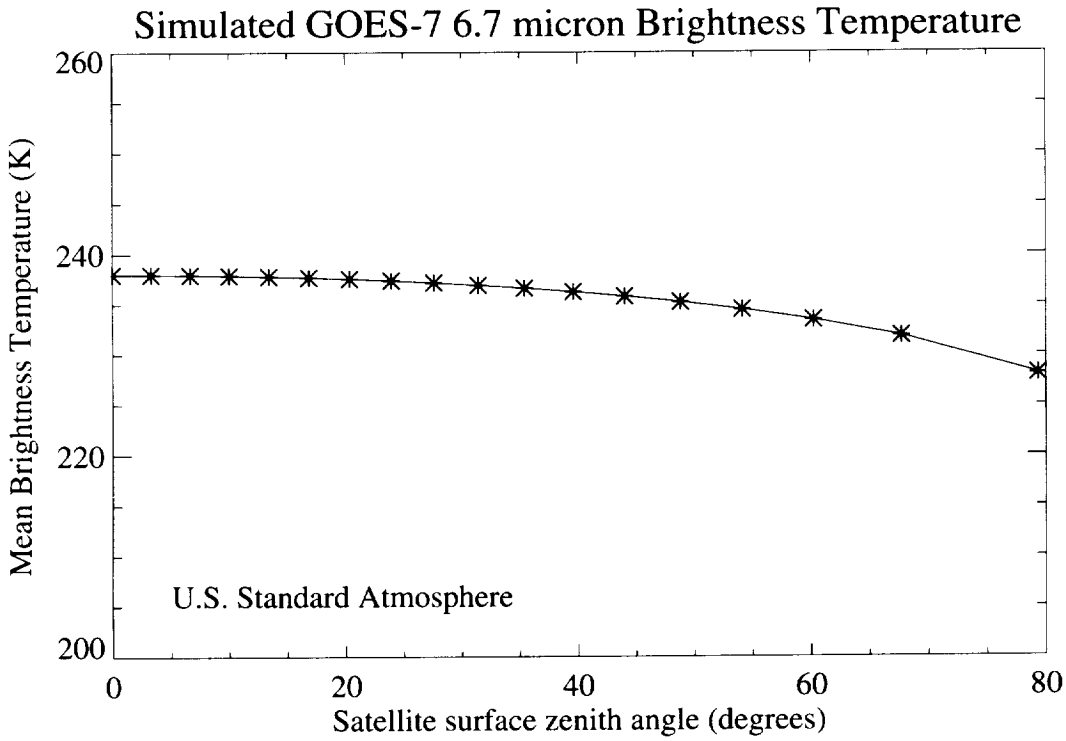

Figure 14: Variation of 6.7 μm brightness temperature with incidence angle for the U.S. standard atmosphere.

6.2 Statistics of the distortion

To test the methodology presented in section 5 a large sample is required. Initially we wish to study the 500 hPa height field only. A convenient collection of forecasts and analyses for this purpose are the Lorenz data sets collected at ECMWF (Lorenz 1982, Simmons *et al.* 1995 [10, 21]). Under the current contract we have acquired these data for four seasons—winter 1981, 1990, 1998; summer 1990. We plan to begin using them to develop statistics of the distortion as soon as the follow-on contract is finalized.

6.3 EOF analysis

To further limit the degrees of freedom used to represent the forecast errors, the displacement and amplification patterns themselves, separately and together, will be analyzed in terms of EOFs or rotated EOFs, to extract the typical modes of the forecast errors. The advantage of rotated EOFs (Richman 1981, 1986 [16, 17]), is that the resulting patterns can be localized. This may help to identify potential causes of model error. The EOF representation may also provide the basis for an enhanced version of J_d.

We will examine the time series of the EOF coefficients of the forecast error displacement and amplification patterns for a fixed forecast length for correlations and periodic behavior. Further we will examine the evolution of forecast errors in these terms for the 1 to 5 day range.

6.4 500 hPa geopotential heights assessment application

The study of the forecast errors of the 500 hPa geopotential height fields will be extended to examine how forecast error varies interannually. With several years worth of data, we will attempt to correlate the forecast failure modes with the large-scale flow pattern and with other factors which might be improperly parameterized or ignored by the model. For example, it would be possible to represent the large scale atmospheric flow pattern and ocean circulation; anomalies in the SST, sea ice, and snow cover fields; and stratospheric volcanic aerosol by simple indices. Then these indices might be correlated with the coefficients of the leading EOFs of the distortion representation of the forecast errors. In this work we might make use of the archived forecasts and analyses of an operational model for several winters. However variations in predictability would then be mixed with variations in model forecast skill. To remove the effects of model changes it would be optimal to use a set of forecasts from one of the reanalysis projects. Currently reanalysis projects are underway at ECMWF, NMC and NASA GSFC. However, a preliminary analysis based on the Lorenz data sets is a logical first step.

References

[1] R. Atlas, R. N. Hoffman, E. Brin, and P. M. Woiceshyn. The impact of ERS-1 scatterometer data on GEOS model forecasts. In *International Symposium on Assimilation of Observations in Meteorology and Oceanography*, pages 573–578, Tokyo, Japan, 13-17 Mar. 1995. WMO TD-651.

[2] A. Berk, L. S. Berstein, and D. C. Robertson. MODTRAN: A moderate resolution model for LOWTRAN 7. Technical Report 89-0122, Air Force Geophysics Laboratory, Hanscom AFB, MA, 1989.

[3] J. E. Dennis, D. M. Gay, and R. E. Welsch. An adaptive nonlinear least-squares algorithm. *ACM Transactions on Mathematical Software*, 7:348–383, 1981.

[4] C. Grassotti, R. N. Hoffman, and H. Iskenderian. Fusion of ground-based radar and satellite-based rainfall data using feature calibration and alignment. *J. Applied Meteorol.*, 1998. In press.

[5] R. N. Hoffman. SASS wind ambiguity removal by direct minimization. II: Use of smoothness and dynamical constraints. *Mon. Weather Rev.*, 112:1829–1852, 1984.

[6] R. N. Hoffman and C. Grassotti. A technique for assimilating SSM/I observations of marine atmospheric storms. *J. Applied Meteorol.*, 35(8):1177–1188, Aug. 1996.

[7] R. N. Hoffman, Z. Liu, J.-F. Louis, and C. Grassotti. Distortion representation of forecast errors. *Mon. Weather Rev.*, 123(9):2758–2770, Sept. 1995.

[8] R. N. Hoffman, J.-F. Louis, and T. Nehrkorn. A simplified view of adjoint calculations in the discrete case. Technical Memorandum 184, Eur. Cent. for Med. Range Weather Forecasts, Reading, England, 1992.

[9] R. N. Hoffman and T. Nehrkorn. A simulation test of three-dimensional retrievals. *Mon. Weather Rev.*, 117:473–494, 1989.

[10] E. N. Lorenz. Atmospheric predictability experiments with a large numerical model. *Tellus*, 34:505–513, 1982.

[11] L. M. McMillin, L. J. Crone, M. D. Goldberg, and T. J. Kleespies. Atmospheric transmittance of an absorbing gas. 4. OPTRAN: a computationally fast and accurate transmittance model for absorbing gases with fixed and with variable mixing ratios at variable viewing angles. *Appl. Opt.*, 34(27):6269–6274, Sept. 1995.

[12] D. Offiler. The calibration of *ERS-1* satellite scatterometer winds. *J. Atmospheric Oceanic Technology*, 11(4):1002–1017, Aug. 1994.

[13] D. F. Parrish and J. C. Derber. The National Meteorological Center's spectral statistical-interpolation analysis system. *Mon. Weather Rev.*, 120:1747–1763, 1992.

[14] D. F. Parrish, J. C. Derber, R. J. Purser, W.-S. Wu, and Z.-X. Pu. The NCEP global analysis system: Recent improvements and future plans. *J. Meteorol. Soc. Japan*, 75(1B):359–365, 1997.

[15] F. Rabier, A. McNally, E. Andersson, et al. The ECMWF implementation of three dimensional variational assimilation (3D–Var). Part II: Structure functions. *Q. J. R. Meteorol. Soc.*, 123, 1997. Submitted.

[16] M. B. Richman. Obliquely rotated principal components: An improved meteorological map typing technique? *J. Applied Meteorol.*, 20:1145–1159, 1981.

[17] M. B. Richman. Rotation of principal components. *J. Climate*, 6:293–335, 1986.

[18] H. Ritchie. Semi-Lagrangian advection on a Gaussian grid. *Mon. Weather Rev.*, 115:608–619, 1987.

[19] J. Schmetz and O. M. Turpeinen. Estimation of the upper tropospheric relative humidity field from METEOSAT water vapor image data. *J. Applied Meteorol.*, 27:889–8989, 1988.

[20] S. D. Schubert, R. B. Rood, and J. Pfaendtner. An assimilated dataset for earth science applications. *Bull. Am. Meteorol. Soc.*, 74(12):2331–2342, Dec. 1993.

[21] A. J. Simmons, R. Mureau, and T. Petroliagis. Error growth and estimates of predictability from the ECMWF forecasting system. *Q. J. R. Meteorol. Soc.*, 121:1739–1771, 1995.

A Required forms

The required Report Documentation Pages (NASA Form 1626 and Standard Form 298) are attached.

REPORT DOCUMENTATION PAGE

Form Approved
OMB No. 0704-0188

1. AGENCY USE ONLY *(Leave blank)*	2. REPORT DATE	3. REPORT TYPE AND DATES COVERED
	August 1998	Contractor Report

4. TITLE AND SUBTITLE
Distortion Representation of Forecast Errors for Model Skill Assessment and Objective Analysis (Annual Report)

5. FUNDING NUMBERS
NAS5-32953
Code 910.3

6. AUTHOR(S)
Ross N. Hoffman (PI), Thomas Nehrkorn, and Christopher Grassotti

7. PERFORMING ORGANIZATION NAME(S) AND ADDRESS (ES)
Atmospheric and Environmental Research, Inc.
840 Memorial Drive
Cambridge, MA 02139

8. PEFORMING ORGANIZATION REPORT NUMBER
P599

9. SPONSORING / MONITORING AGENCY NAME(S) AND ADDRESS (ES)
National Aeronautics and Space Administration
Washington, DC 20546-0001

10. SPONSORING / MONITORING AGENCY REPORT NUMBER
CR-1998-208602

11. SUPPLEMENTARY NOTES
Technical Monitor: S, Cohn, Code 910.3

12a. DISTRIBUTION / AVAILABILITY STATEMENT
Unclassified–Unlimited
Subject Category: 46
Report available from the NASA Center for AeroSpace Information,
7121 Standard Drive, Hanover, MD 21076-1320. (301) 621-0390.

12b. DISTRIBUTION CODE

13. ABSTRACT *(Maximum 200 words)*

We proposed a novel characterization of errors for numerical weather predictions. A general distortion representation allows for the displacement and amplification or bias correction of forecast anomalies.

Characterizing and decomposing forecast error in this way has several important applications, including the model assessment application and the objective analysis application. In this project, we have focused on the assessment application, restricted to a realistic but univariate 2-dimensional situation. Specifically, we study the forecast errors of the sea level pressure (SLP), the 500 hPa geopotential height, and the 315K potential vorticity fields for forecasts of the short and medium range. The forecasts are generated by the Goddard Earth Observing System (GEOS) data assimilation system with and without ERS1 scatterometer data.

A great deal of novel work has been accomplished under the current contract. In broad terms, we have developed and tested an efficient algorithm for determining distortions. The algorithm and constraints are now ready for application to larger data sets to be used to determine the statistics of the distortion as outlined above, and to be applied in data analysis by using GEOS water vapor imagery to correct short-term forecast errors.

14. SUBJECT TERMS	15. NUMBER OF PAGES
Numerical Weather Prediction, Forecast Errors, GEOS	28
	16. PRICE CODE

17. SECURITY CLASSIFICATION OF REPORT	18. SECURITY CLASSIFICATION OF THIS PAGE	19. SECURITY CLASSIFICATION OF ABSTRACT	20. LIMITATION OF ABSTRACT
Unclassified	Unclassified	Unclassified	UL